

1 **Comparison of measured brightness temperatures from**
2 **SMOS with modelled ones from ORCHIDEE and H-TESSEL**
3 **over the Iberian Peninsula**

4

5 **A. Barella-Ortiz^{1,5}, J. Polcher^{1,5}, P. de Rosnay², M. Piles³ and E. Gelati^{4,5}**

6 [1]{Laboratoire de Météorologie Dynamique du CNRS, IPSL, École Polytechnique,
7 Université Paris-Saclay, France}

8 [2]{European Centre for Medium-Range Weather Forecasts, Reading, UK}

9 [3]{Dept. de Teor. del Senyal i Comunicacions, Univ. Politec. de Catalunya, Barcelona,
10 Spain}

11 [4]{CNRM-GAME (Météo-France, CNRS), Toulouse, France}

12 [5]{Centre National de la Recherche Scientifique (CNRS)}

13 Correspondence to: A. Barella-Ortiz (Anais.Barella-ortiz@lmd.jussieu.fr)

14

15 **Abstract**

16 L-Band radiometry is considered to be one of the most suitable techniques to estimate Surface
17 Soil Moisture (SSM) by means of remote sensing. Brightness temperatures are key in this
18 process, as they are the main input in the retrieval algorithm which yields SSM estimates. The
19 work exposed compares brightness temperatures measured by the SMOS mission to two
20 different sets of modelled ones, over the Iberian Peninsula from 2010 to 2012. The latter were
21 estimated using a radiative transfer model and state variables from two land surface models: i)
22 ORCHIDEE and ii) H-TESSEL. The radiative transfer model used is the CMEM.

23 Measured and modelled brightness temperatures show a good agreement in their temporal
24 evolution, but their spatial structures are not consistent. An Empirical Orthogonal Function
25 analysis of the brightness temperature's error identifies a dominant structure over the South-
26 West of the Iberian Peninsula which evolves during the year and is maximum in fall and
27 winter. Hypotheses concerning forcing induced biases and assumptions made in the radiative
28 transfer model are analysed to explain this inconsistency, but no candidate is found to be

1 responsible for the weak spatial correlations at the moment. Further hypotheses are proposed
2 and will be explored in a forthcoming paper.

3 **1 Introduction**

4 The United Nations (UN), the Food and Agriculture Organization (FAO), and the World
5 Health Organization (WHO), have reported that water resources are not being managed in an
6 optimum way at present. As a result, scarcity, hygiene and pollution issues related to
7 improper water policies are detected. In addition, the world's population is expected to grow
8 by 2 to 3 billion people over the next 40 years according to the UN's World Water
9 Development Report from 2012 (WWAP, 2012). This will lead to a significant increase in
10 freshwater demand which will likely be affected by the effect of a changing climate.

11 To achieve a better management of water resources, it is necessary to improve our
12 understanding of hydrological processes. In order to do this, the study of Soil Moisture (SM)
13 is essential. It is defined as the water content in the soil and has a key role on the soil-
14 atmosphere interface. SM determines whether evaporation over land surfaces occurs at a
15 potential rate (controlled by atmospheric conditions) or if it is limited by the available
16 moisture (Milly, 1992). In addition, it influences several processes, like infiltration and
17 surface temperature, which have an important effect on plant growth and the general state of
18 the continental surfaces. However, SM is a complex variable to model as the interactions
19 between soils and water are not simple to represent. Its definition requires knowledge of soil
20 hydraulic properties, which are not often available as direct measurements. Pedo-transfer
21 functions (Marthews et al., 2014), allow to estimate hydrodynamic characteristics of the soil
22 from available soil texture and structure information. However, the suitability of these
23 functions is under debate (Baroni et al., 2008), as their performance depends on several
24 factors like the climate, geology, and the measurement techniques used. Furthermore,
25 different hydrological schemes are found in Land Surface Models (LSM), leading to various
26 ways of understanding and formulating soil moisture.

27 Remotely sensed soil moisture products have brought about new ways to perform data
28 retrieval, adding new observations to data assimilation chains. The optimal combination of
29 these products with modelled ones is expected to provide better estimates of the true soil
30 moisture state. Remote sensing allows to estimate SM by means of retrieval algorithms, like
31 inversion algorithms (Kerr et al., 2012) or neural networks (Kolassa et al., 2013). Their main
32 input depends on the type of sensor used. This is, backscattering for an active sensor and

1 Brightness Temperature (TB) for a passive sensor. TB corresponds to the radiance emitted by
2 the Earth at a given wavelength and is the magnitude measured by a radiometer. It is defined
3 as the physical temperature times the emissivity of the surface.

4 L-Band radiometry is one of the best methods to estimate soil moisture, due to the relation
5 between SM and the soil dielectric constant (ϵ) in this wavelength. The latter differs
6 significantly between a dry soil and water (4 vs. 80, respectively) and this difference is key to
7 estimate the soil water content. It should be noted that the retrieved SM corresponds to the
8 water contained in the first centimetres of the soil. The penetration depth in averaged
9 conditions is about 5 cm (Kerr et al., 2010). Therefore, we will refer to Surface Soil Moisture
10 (SSM) instead of soil moisture. Some studies, like Escorihuela et al. (2010) lower the
11 penetration depth to 1–2 cm.

12 In the last decade, three space missions have been launched with L-Band radiometers on-
13 board: the Soil Moisture and Ocean Salinity (SMOS) mission (Kerr et al., 2010), the
14 Aquarius/SAC-D mission (Le Vine et al., 2010), and the Soil Moisture Active and Passive
15 (SMAP) mission (Entekhabi et al., 2010).

16 A large number of validation studies of remotely sensed SSM products have been carried out
17 (Albergel et al., 2011; Sánchez et al., 2012; Bircher et al., 2013). These studies are usually
18 performed using airborne and or ground-observed data over a well equipped site. Other
19 studies, like the one described in González-Zamora et al. (2015), validate SMOS SSM
20 products using in situ soil moisture measurement networks, which allow to extend the study
21 period to annual and inter-annual scales. Several studies have been performed to validate
22 brightness temperatures too (Rüdiger et al., 2011; Montzka et al. 2013). In Bircher et al.
23 (2013) TBs are also validated with network and airborne data over a SMOS pixel in the
24 Skjern river Catchment (Denmark). LSMs coupled to Radiative Transfer Models (RTMs) can
25 contribute to the analysis and validation of passive Microwave (MW) data. Models permit
26 extending the validation to a longer period of time and perform an extensive analysis of
27 observed and retrieved data, as shown in Schlenz el al. (2012). In this study, they compare
28 TBs and vegetation optical depth from SMOS with modelled ones obtained from a LSM
29 coupled to a radiative transfer model, over a period of seven months in 2011 in the Vils test
30 site (Germany). Comparing modelled with satellite-measured brightness temperatures can
31 help to better understand inconsistencies between retrieved and modelled data. It provides

1 information regarding the origin of their differences, and whether they are due to the retrieval
2 algorithm or to issues related to the modelling process.

3 Polcher et al. (2015) present the first comparison of the spatial patterns of Level 2 (L2) SMOS
4 product corresponding to retrieved SSM, with SSM modelled by the ORganising Carbon and
5 Hydrology In Dynamic EcosystEms (ORCHIDEE) LSM (de Rosnay and Polcher, 1998;
6 Krinner et al., 2005) over the Iberian Peninsula (IP) from 2010 to 2012. They have identified
7 inconsistencies between the spatial structures of retrieved and modelled SSM. The main
8 objective of the work presented herein is to extend the analysis of this inconsistency by
9 comparing brightness temperatures measured by SMOS (Level 1C, L1C, product) with
10 modelled ones obtained from the coupling of ORCHIDEE's state variables and a RTM. In
11 addition, a second set of modelled TBs using state variables from the Hydrology – Tiled
12 ECMWF Scheme for Surface Exchanges over Land (H-TESSEL), is included in the
13 comparison. The RTM used is the Community Microwave Emission Model (CMEM) [de
14 Rosnay et al., 2009], developed by the European Centre for Medium-Range Weather
15 Forecasts (ECMWF). The comparison is performed over the same period and region as the
16 study carried out by Polcher et al. (2015). The IP is an excellent test case for remote sensing
17 of SSM, as its two characteristic climate regimes (oceanic and Mediterranean) result in a
18 strong contrast in soil water content. Furthermore, SSM is a critical variable regarding water
19 resources especially in the IP, which makes this study even more necessary.

20 The data from SMOS and the LSMs used in this paper will be presented in the next section.
21 Next, a methodology section will follow, describing the data filtering and sampling processes
22 carried out, together with the analysis performed to compare TBs. Afterwards, results will be
23 presented. First, modelled and measured TBs will be compared. Secondly, their error will be
24 characterised spatially and temporally and certain hypotheses to explain the differences found
25 in the TB comparison will be analysed. Finally, we will study the amplitude of the annual
26 cycle of the TB signals. The paper will end with discussion and conclusion sections.

27 **2 Data**

28 **2.1 SMOS retrievals of TB**

29 The SMOS mission is the second Earth Explorer Opportunity mission from the European
30 Spatial Agency (ESA). The SMOS satellite was launched on November 2nd, 2009. One of its

1 main objectives is to provide surface soil moisture over land with a target accuracy of 0.04
2 m^3m^{-3} .

3 As previously said, TBs are the main input of SMOS's soil moisture retrieval algorithm. L-
4 band brightness temperatures are measured by the SMOS radiometer at different incidence
5 angles (from 0 to 65°) and polarizations (H, V, HV). The retrieval algorithm also models TBs
6 using the state-of-the-art L-band Microwave Emission of the Biosphere (L-MEB) forward
7 model (Wigneron et al., 2007) with some modifications. These brightness temperatures are
8 then used to retrieve SSM using an inversion algorithm based on an iterative approach. Its
9 objective is to minimize the sum of the squared weighted differences between measured and
10 modelled TBs for all available incidence angles. Details about the retrieval algorithm are
11 provided in Kerr et al. (2012).

12 The SMOS L1C v5.05 product over the 10W : 5W to 45N : 35N region was selected and
13 SMOS TBs at the antenna reference plane were derived: TBs are first screened out for Radio-
14 Frequency Interferences (RFIs) (strong, point source and tails), and also for Sun (glint area,
15 aliases and tails), and Moon (aliases) contamination, using the corresponding flags.
16 Ionospheric effects (geometric and Faraday rotations) are later corrected to obtain TB at the
17 Top Of the Atmosphere (TOA). TB maps at a constant incidence angle of $42.5 \pm 5^\circ$ are
18 obtained through chi squared linear fit of all values included in the interval $42.5 \pm 5^\circ$, which is
19 the methodology used to generate the SMOS L1C browse product (McMullan et al., 2008).
20 Finally, these maps are resampled from the Icosahedral Snyder Equal Area (ISEA) 4H9 grid
21 to a 0.25° regular latitude-longitude grid, to facilitate its manipulation.

22 The L1C product containing horizontally and vertically polarized brightness temperatures,
23 was provided by the SMOS Barcelona Expert Center. From now on, this product will be
24 referred to as TB_{SM} .

25 **2.2 Modelled TB: CMEM**

26 The Community Microwave Emission Modelling (CMEM) Platform,
27 (<https://software.ecmwf.int/wiki/display/LDAS/CMEM>) developed at ECMWF, is a forward
28 operator for low frequency passive MW brightness temperatures of the surface. Its physics is
29 based on that of the L-MEB forward model and the Land Surface Microwave Emission Model
30 (LSMEM) [Drusch et al., 2001]. CMEM is characterized by its modular structure, which
31 allows the user to choose among different physical configurations to compute TB's key

1 parameters. Polarized brightness temperatures provided at TOA result from the contribution
2 of three dielectric layers: atmosphere, soil and vegetation. Snow, also considered, is
3 characterized as a single additional homogeneous layer.

4 The two sets of modelled TBs used in this study were estimated by means of the CMEM
5 provided with state variables from i) ORCHIDEE, and ii) H-TESSEL simulations. From now
6 on we will refer to these sets as TB_{OR} and TB_{HT} , respectively. TB_{OR} was computed
7 specifically for this study, while TB_{HT} was provided by the ECMWF to widen the comparison
8 between measured and modelled data. The CMEM configuration used to compute each set of
9 TB is listed in Table 1. The table is divided into three configuration categories: physical,
10 observing, and soil and atmospheric levels. Even though both sets have similar
11 configurations, there are some differences which are explained below.

12 First, the “Physical configuration” of TB_{OR} was selected to be as similar as possible to TB_{HT} .
13 However, they differ in the parameterization used to compute the smooth surface emissivity
14 (ϵ_s). For TB_{HT} the reflectivity of the flat soil surface was computed following the Fresnel law
15 (Ulaby et al., 1986), so it is expressed as a function of the soil dielectric constant and the
16 observation incidence angle. This formulation considers the emission at the soil interface. As
17 it is simple and affordable in computing time it is commonly used for microwave emission
18 modelling and soil moisture retrieval, as well as for operational applications (e.g. Wigneron et
19 al., 2007, de Rosnay et al., 2009). It assumes an a priori soil moisture sampling depth, which
20 in this study corresponds to the first soil layer of the land surface model (7cm for H-
21 TESSEL). For TB_{OR} , the multilayered soil hydrology of ORCHIDEE allows to take into
22 account the soil moisture profile and the resulting volume scattering effects on the soil
23 emission. Therefore the reflectivity of the flat soil surface was computed using the
24 parameterization proposed by Wilheit (1978). The different parameterizations chosen to
25 calculate ϵ_s lead to another variation between the CMEM configurations. If ϵ_s is computed
26 using Wilheit (1978), the soil temperature profile is used to compute the Effective
27 Temperature (T_{eff}). On the contrary, if the Fresnel law is used, the user can choose among
28 different parameterizations to compute T_{eff} . For TB_{HT} , Wigneron et al. (2001) was selected.

29 Second, the “Observing configuration” considers different incidence angles for each set.
30 Although the available TB_{HT} were modelled considering an angle of 40° , 42.5° was used to
31 model TB_{OR} , because measured TBs were provided at this angle.

1 Third, a different number of soil layers was defined for the “Soil and atmospheric level
2 configuration”: 11 (TB_{OR}) and 3 (TB_{HT}). ORCHIDEE’s soil discretization is finer. For
3 instance, its first layer’s depth is of the order of millimetres, while H-TESSEL’s is of
4 centimetres. In order to evaluate the role of these differences in the vertical discretization and
5 the LSMs, we performed a sensitivity analysis as detailed in the next paragraph.

6 In addition to the CMEM simulations performed to model TB_{OR} and TB_{HT} using the
7 configurations indicated in Table 1, the following simulations were carried out to test if
8 parameterization assumptions could affect the resulting TBs:

- 9 • Simulation 1: $TB_{HT(VC)}$, where the subscript “VC” stands for “Vegetation Cover”.

10 Vegetation cover is a key input. Since this parameter is directly related to land-surface
11 emissivity, the effects of a different vegetation cover were tested on TB_{HT} . For this
12 matter, a new set of TBs was modelled using H-TESSEL’s state variables with the
13 same configuration as detailed in Table 1, except for the vegetation cover input, where
14 H-TESSEL’s prescribed vegetation (Boussetta et al., 2013) was considered. One of the
15 differences between this input and the ECOCLIMAP database (used in the original
16 configuration), is that the former consists of 20 vegetation types, while the latter
17 considers 7.

- 18 • Simulation 2: $TB_{OR(SD)}$, where the subscript “SD” stands for “Soil Discretization”,

19 The impact of a coarser soil discretization on modelled TBs was tested by
20 recomputing TB_{OR} using ORCHIDEE’s state variables averaged to 3 soil layers: upper
21 (9 cm), medium (66 cm), and lower (125 cm).

- 22 • Simulation 3: $TB_{OR(FW)}$, where the subscript “FW” stands for “Fresnel Wigneron”.

23 We tested the combined effect of using the Fresnel law to compute ϵ_s , rather than the
24 parameterization proposed by Wilheit (1978), and calculating T_{eff} using the
25 methodology proposed by Wigneron (2001) instead of the soil temperature profile. For
26 this, TBs were simulated using ORCHIDEE’s state variables.

27 The input variables required by the CMEM to model TBs are summarized in Table 2. They
28 are classified into dynamic and constant fields and consist of meteorological data, vegetation
29 characteristics and soil conditions.

2.2.1 The ORCHIDEE and H-TESSEL Land Surface Models

2 The ORCHIDEE LSM (de Rosnay and Polcher, 1998; Krinner et al., 2005) was developed by
3 the Institut Pierre – Simon Laplace (IPSL). It can be run coupled with the general circulation
4 model LMDZ, which was developed by the Laboratoire de Météorologie Dynamique (LMD),
5 or in stand-alone mode. Uncoupled simulations were carried out for this study.

6 The hydrological scheme used by ORCHIDEE approaches hydrology through the resolution
7 of a diffusive equation with a multilayer scheme. For this, the Fokker-Planck equation is
8 solved over a soil 2 m deep with an 11 layer discretization. The layers' depths are informed in
9 Table 1. The lower boundary condition is free drainage, under the hypothesis that the water
10 content gradient between the last modelled layer and the next one (not modelled) is zero. The
11 upper boundary condition sets the bare soil evaporation as the maximum upward hydrological
12 flux which is permitted by diffusion if it is lower than potential evaporation

13 The multilayer scheme considers a sub-grid variability of soil moisture, which together with
14 the fine soil discretization improves the representation of infiltration processes. The soil
15 infiltration follows the Green-Ampt equation (Green and Ampt, 1911) to represent the
16 evolution in time of the wetting front through the soil layers. It should be noted that partial re-
17 infiltration occurs from surface runoff if the local slope of the grid-cell is $\leq 0.5\%$ (D'Orgeval
18 et al., 2008). Each grid box has a unique soil texture and structure (Post and Zobler, 2000),
19 but three different soil columns are considered, each one with its own soil moisture
20 discretization and root profile. These are classified as: bare soil, low and high vegetation
21 regrouping the 13 Plant Functional Types (PFT) defined in ORCHIDEE. These PFTs
22 contribute to the soil layers of each grouping a root density to compute extraction and soil
23 moisture stress to the plants. The water balance is solved for each soil column resulting in
24 three different soil moisture profiles in each grid box.

25 ORCHIDEE's soil temperature profile is calculated solving the heat diffusion equation.
26 Contrary to the hydrological scheme, it considers a 7 layer discretization, where the layers'
27 thicknesses follow a geometric series of ratio 2, and a total soil depth of 5.5 m (Hourdin,
28 1992; Wang et al., 2016). For this study, the first 2 m of the temperature profile were
29 calculated following the same soil discretization as the one considered in the soil moisture
30 calculation. The energy balance takes into account the skin temperature as presented in Schulz
31 et al. (2001) to derive the Land Surface Temperature (LST). The soil and vegetation are
32 considered as a single medium assigned with a surface temperature (Santaren et al., 2007).

1 The H-TESSEL LSM (Balsamo et al., 2009), developed by the ECMWF, revises and
2 improves certain aspects regarding the soil hydrology of the TESSEL model. Its hydrology
3 scheme solves a diffusive equation over a multilayer scheme with a 4 layer discretization.
4 Layer depths follow an approximate geometric relation (Table 1). In addition, the soil can be
5 covered by a single snow layer. H-TESSEL considers the same lower boundary condition as
6 ORCHIDEE. However, it differs in the upper one that accounts also for infiltration. It defines
7 a maximum infiltration rate given by the maximum downward diffusion from the saturated
8 surface. Once this rate is exceeded by the water flux at the surface, the excess of water is
9 derived to surface runoff.

10 The model considers six types of tiles over land: bare soil, low and high vegetation, water
11 intercepted by leaves, as well as shaded and exposed snow. Each one of these has its own
12 energy and water balance. However, only one soil moisture reservoir is considered. Recent
13 improvements have replaced a globally uniform soil type (loamy) by a spatially varying one
14 (coarse, medium, medium-fine, fine, very fine, organic). Surface runoff, based on variable
15 infiltration capacity, was also a recent improvement.

16 H-TESSEL's soil temperature profile is computed using the same soil discretization as the one
17 defined in its hydrological scheme. The soil heat budget follows a Fourier diffusion law,
18 which has been modified to consider also thermal effects caused by changes in the soil water
19 phases (Holmes et al., 2012). To simulate the LST, a skin layer is defined representing i) the
20 layer of vegetation, ii) the top layer of bare soil, or iii) the top layer of the snow pack. The
21 surface energy balance equation is then linearised for each tile (Viterbo and Beljaars, 1995).

22 Both LSMs are forced with the ERA-Interim forcing (Dee et al. 2011), which is suitable for
23 this study because it ranges from 1979 to 2012 and recent data were needed to perform the
24 comparison with SMOS's. We are aware that biases in this kind of forcings have an effect on
25 the LSMs simulations (Ngo-Duc et al., 2005). ORCHIDEE was configured to output hourly
26 TB values. However, TB_{HT} is only available at 6 hourly time steps (at 00, 06, 12, and 18
27 hours). Due to this difference, each set of modelled TBs was sampled in a different way to
28 approximate TB_{SM} measurement times. The sampling processes will be explained in Section
29 3.

30 The above paragraphs show that the hydrology, soil processes and land surface temperatures
31 are approached very differently by both models. Therefore, the impact of these differences
32 needs to be considered when comparing simulated TBs.

1 **2.3 Precipitation and Land Surface Temperature**

2 One important common feature of the presented model simulations is the forcing data. Since
3 biases in the imposed atmospheric conditions can affect modelled TBs, it was decided to
4 validate two important variables for which independent observations exist. Focus was put on
5 Precipitation (P) and the Land Surface Temperature (LST), as they are key variables for the
6 water and radiative balances.

7 P is the main driver of SSM, and this directly drives the L-Band emissivity. According to
8 Zollina et al. (2004), P generated by a reanalysis (like ERA-Interim which is used here) is
9 highly model dependent and one of the less reliable forecast parameters since models do not
10 represent accurately all the physical processes of the atmospheric water cycle. Therefore, the
11 verification of this forcing variable of the LSMs with independent data is essential.

12 As for the radiative balance, the available energy at the surface is one of the major drivers of
13 LST. We chose to verify this variable in this study for two reasons. First, it provides a good
14 summary of the surface energy balance. Second, it is a key parameter in CMEM's estimation
15 of TB. Therefore, its analysis will indicate whether the LSM thermodynamics shows biases
16 with spatio-temporal characteristics similar to those from TBs.

17 The independent datasets used for validation are:

- 18 • P from the E-OBS dataset (Haylock et al., 2008),
- 19 • LST provided by the LandSAF product (<http://landsaf.meteo.pt>).

20

21 **3 Methods**

22 **3.1 Data sampling and filtering processes**

23 To compare modelled and measured brightness temperatures, TB_{OR} and TB_{HT} were sampled
24 with TB_{SM} and remapped to the nearest neighbour of the SMOS grid. This allows to keep the
25 spatial structures of the coarse model resolution. Next, the three TB signals were filtered to
26 exclude certain situations, such as frozen soils or RFIs, which are known to make SSM
27 estimates unreliable.

1 3.1.1 Sampling

2 The objective of sampling the data is to use only modelled TBs corresponding to available
3 measured values. TB_{OR} were sampled at an hourly scale. However, TB_{HT} consists of 6 hourly
4 values, thus potentially resulting in a large number of neglected data because TB_{HT} and
5 SMOS time steps did not always correspond. Therefore, TB_{HT} were sampled considering a 3
6 hour window around the observation in order to keep a larger number of modelled data for the
7 comparison. To test the impact of this approximation, we also applied it to the TB_{OR} and
8 compared it to the original hourly data. Differences between them were under 0.1% for the
9 diagnostics used here, and thus, it was considered to be negligible.

10 3.1.2 Filtering

11 Data was filtered to discard unreasonable TB values from the comparison study. Filtering
12 rules were devised following the ECMWF criteria used to screen TB_{HT} (Table 3). Common
13 filters were also applied to measured and modelled TBs.

14 The filters applied in TB_{HT} corresponding to the water content in snow cover (snow water
15 equivalent) and the criterion on ERA-Interim's 2 m air temperature aim to discard frozen
16 soils, which might affect the SM retrieval (Dente et al., 2012). The same result was achieved
17 by filtering TB_{OR} with the 2 m temperature from the forcing (as in the previous case) as well
18 as with ORCHIDEE's average surface temperature. The first common criterion excludes TBs
19 higher than 300 K to avoid effects of RFIs, which can result in overestimated brightness
20 temperatures (higher than 1000K). The second common criterion aims at removing points
21 which might be influenced by coastal or topographic effects, as does H-TESSEL's orography
22 (slope) criterion too. The mask was built using the L2 SMOS product. Any pixel with no
23 surface soil moisture data retrieved, together with the 24 pixels surrounding it, was excluded
24 from the comparison.

25 **3.2 Comparison analyses**

26 3.2.1 Spatio-temporal correlation

27 The first diagnostic performed to compare measured and modelled TBs consisted in temporal
28 and spatial correlation analyses. Our aim is to study the similarity between the spatio-
29 temporal patterns. We used the Pearson product-moment correlation coefficient. Only values

1 statistically significant at the 95% level are considered. An averaging window of 5 days is
2 applied for the spatial correlation analysis to ensure the highest coverage possible.

3 Even though the correlation coefficient is a widely used statistical tool, it may not be suitable
4 when analysing certain fields. For instance, Polcher et al. (2015) showed that temporal
5 correlation measured between remotely sensed, in-situ, and modelled SSM, is mainly driven
6 by the high frequency behaviour of SSM. Therefore, this diagnostic is not very sensitive to
7 the slower variations of the field studied. Performing the correlation analyses allowed us to
8 study if this conclusion also applies to TBs.

9 3.2.2 Empirical Orthogonal Function

10 The Empirical Orthogonal Function (EOF) analysis extracts the dominant spatial and
11 temporal modes of variability of a field. It relates the spatial patterns of each variation mode
12 with a time series and its explained variance. We will refer to the time series of each variation
13 mode as the Expansion Coefficients (ECs). They provide information about the spatial
14 pattern's temporal evolution. Positive values of ECs imply that there is no sign change in the
15 patterns. The EOF methodology is detailed in Björnsson and Venegas, (1997) for instance.

16 We apply the EOF analysis to the error between measured and modelled TBs, to characterize
17 it spatially and temporally. Identifying the main modes of variability of an error field allows
18 to propose and test hypotheses about its causes. We will follow this approach to analyse the
19 impact of forcing biases on modelled TBs. Other studies have also applied this methodology
20 to error analysis. For example, Kanamitsu et al. (2010) analyze the impact of a regional model
21 error on the inter-annual variability of a set of analysis fields.

22 4 Results

23 The temporal evolution and spatial structures of measured and modelled TBs are analysed in
24 this section. This study follows the comparison between modelled and retrieved SSM
25 (Polcher et al., 2015) and attempts to elucidate if the difference found can be attributed either
26 to the retrieval algorithm, which converts TBs into estimated SSM, or its modelled
27 counterpart.

28 4.1 Comparison of modelled and measured TBs

29 The mean temporal and spatial correlations between measured and modelled TBs, over the IP
30 from 2010 to 2012, are shown in Table 4. Values from the SSM comparison performed by

1 Polcher et al. (2015) are also included. The differences between spatial and temporal
2 correlation are already apparent and warrant separate analyses as a first step.

3 4.1.1 Temporal correlation

4 Fig. 1 shows the temporal correlation between measured and modelled daily TBs for the
5 horizontal and vertical polarizations. Both polarizations show a good agreement between
6 models and observations in their temporal evolution, with values above 0.7 over a large part
7 of the IP. This can be explained by the strong annual cycle imposed by the surface
8 temperature, but more important are the quick responses of temperature and emissivity to
9 precipitation events, which drive TB's fast variations and correspond to the synoptic
10 variability of the signal. The high correlations indicate that it is well captured by both models.
11 Most of the areas with lower correlations correspond to mountain ranges. Relief effects on
12 MW radiometry over land (Mätzler and Standley, 2000) are a difficult remote sensing
13 problem and thus, discrepancies are expected. In fact, the lowest correlations (0.3 to 0.6)
14 appear over some areas of the Pyrenees. Other examples are the Iberian System and the
15 Cantabrian Mountains, located over the North-Eastern and the Northern regions of the
16 peninsula, respectively.

17 There are no large differences between the temporal correlation maps of TB_{OR} and TB_{HT} with
18 TB_{SM} (Fig. 1). Since the same forcing was used, the two LSMs share the same synoptic
19 variability from the ERA-Interim reanalysis. However, Fig. 1 shows that the synoptic
20 variability of H-TESSEL leads to slightly higher correlation values than ORCHIDEE's,
21 especially over the northern part of the IP.

22 4.1.2 Spatial correlation

23 For clarity, the 5 daily spatial correlations are averaged per season and the distribution of
24 values obtained is represented in a boxplot form in Fig. 2. In general, the correlation is poor
25 throughout the year. Although maxima are around 0.6, the annual mean ranges between 0.2
26 and 0.3 (Table 4). This implies that the spatial structures from both modelled TBs are not
27 consistent with those observed by SMOS. We would like to point out the seasonality in the
28 correlation. The lowest correlations occur during winter, where even negative values are
29 obtained. These improve during spring and summer, and weaken again in fall. Moreover,
30 winter and fall generally show larger ranges of variability and thus, a wider dispersion of the
31 data than spring and summer. Fig. 2 also shows that the vertical polarization has

1 systematically higher mean correlations than the horizontal one, except for the winter season.
2 Finally, there is no significant difference in the correlation of TB_{SM} with either modelled TB
3 as has already been noted for the temporal correlation.

4 **4.2 Spatial and temporal characterization of the TB error**

5 The spatio-temporal variability of the error between modelled and measured TBs is studied to
6 better understand the poor consistency of their spatial structures. We want to analyse if this
7 difference can be related to some physical process which might be incorrectly represented in
8 both models. For this, an EOF analysis of the TB errors ($TB_{OR} - TB_{SM}$ and $TB_{HT} - TB_{SM}$) is
9 carried out.

10 **4.2.1 TB error**

11 *Spatial patterns*

12 Fig. 3 shows the spatial patterns of the first two EOF variation modes correspondent to the TB
13 error of ORCHIDEE ($TB_{OR} - TB_{SM}$), for the horizontal and the vertical polarizations. The
14 variance explained by each mode is also provided as a percentage in brackets. The total
15 variance explained by the patterns of the first variation mode is above 30% in both
16 polarizations: 36% (horizontal) and 31% (vertical). These two patterns show a similar
17 structure characterised by high values over the South-West and a smaller area further North of
18 the IP, which weaken as they extend through the rest of the peninsula. This similarity is
19 confirmed by their high spatial correlation, which is 0.99 (Table 5). The second variation
20 mode exhibits a structure that is also maximum over the South-West of the IP in both
21 polarizations. However, the total variance explained is reduced to 6% and 7% (horizontal and
22 vertical polarization, respectively).

23 Fig. 4 is equivalent to Fig. 3 but presents the TB error of H-TESSEL ($TB_{HT} - TB_{SM}$). The
24 variance fractions explained by the first EOF mode are 30% and 18% for the horizontal and
25 vertical polarization, which are lower than those obtained for the TB error of ORCHIDEE. As
26 in Fig. 3, the first variation modes show similar spatial structures, which are highly spatially
27 correlated (0.86, Table 5). It is interesting to note that this structure coincides with the one
28 identified for the TB error of ORCHIDEE (Fig. 3 a and c). This is confirmed by the high
29 correlation obtained between the patterns of the two errors: 0.92 and 0.73 for the horizontal
30 and vertical polarization, respectively (Table 5). The second variation mode of H-TESSEL's

1 TB error explains 8% (horizontal polarization) and 12% (vertical polarization). The horizontal
2 polarization pattern shows that the error is maximum over the South-Western region of the IP,
3 while the vertical polarization pattern does not show a clear structure. Contrary to the first
4 variation mode, patterns from the second one show larger differences with the patterns
5 depicted by the TB error of ORCHIDEE.

6 *Expansion coefficients*

7 Fig. 5 shows the ECs of the first EOF variation mode of both TB errors. Therefore, the
8 projection of the error time series on the EOF pattern, summarizing how much the error field
9 varies according to the pattern.

10 The four series show a strong annual variation which peaks in fall. High values are also
11 observed in December 2012 and during the winter 2010 - 2011. It should be noted that the
12 behaviour of the ECs coincides with the marked seasonality shown in Fig. 2 and thus,
13 reinforces our observation that modelled TB patterns have their strongest disagreement with
14 SMOS measurements in fall and winter. The ECs of the second EOF variation mode of each
15 TB error have not been included in Fig. 5, because the spatial patterns of each error differ
16 between them. Nevertheless, it is important to note that they show variations at higher
17 frequency than those from the first mode.

18 Two conclusions can be drawn from these results:

19 First, the largest spatially coherent error identified in Fig. 3 and 4 (a and c) is dominated by
20 the slow varying component of the TB signals, which is driven by the annual cycle. At first
21 sight, this might seem to contradict the temporal correlation analysis (Fig. 1). However, it
22 evidences that the slow (annual cycle) and fast (synoptic variability) components of TBs show
23 different behaviours. In addition, it confirms our hypothesis that the temporal correlation of
24 TB is driven by its synoptic variability, as demonstrated in the SSM comparison performed by
25 Polcher et al. (2015).

26 Second, modelled TBs are warmer than measured ones over South-Western IP during fall and
27 winter, as revealed by the first EOF patterns and their oscillations (Fig. 3 to 5). To further
28 analyze this result, we looked at ECMWF's mean first guess departure from the months of
29 November 2010 to 2012. This diagnostic consists of the time averaged geographical mean of
30 the difference between SMOS measured TBs and modelled ones using the CMEM and H-
31 TESSEL's surface state variables (Fig. 6). For all three years we see a contrast between the

1 error over the North-Western region of the IP (in an orange colour) and over the South-
2 Western region and a smaller area further North (in a blue colour). According to this,
3 measured TBs are warmer than modelled ones over the North-West of the IP during these
4 three periods, while modelled TBs are warmer than SMOS's over the South-West of the IP.
5 This is in good agreement with the behaviour described by the first EOF variation mode of
6 both TB errors (Fig. 3 and 4, a and c). It should be noted that the mean first guess departure
7 shows a global bias between the spatial patterns of measured and modelled TBs. However,
8 only the IP is represented in this figure to show clearly the spatial structures.

9 To sum up, the EOF analyses of the two TB errors identified a common dominant structure,
10 which is maximum in the fall and winter seasons, over the South-West of the IP and a smaller
11 area further North. It represents between 18% and 36% of the error depending on the
12 modelled TB set considered and its polarization. Moreover, it corresponds well with the
13 ECMWF mean first guess departure for the 2010-2012 November months.

14 4.2.2 LST and Precipitation errors

15 Precipitation and LST data are used to explore possible causes for the difference between
16 measured and modelled TBs. Errors are calculated with respect to independent datasets. The
17 dominant error pattern of each variable is computed via EOF analysis and compared with the
18 dominant pattern of the two TB errors. If similarities can be identified, then possible causal
19 links between these variables and the TB error can be explored.

20 The precipitation error was calculated as the difference between the P provided by the ERA-
21 Interim forcing and the E-OBS independent dataset. The LST errors were computed as the
22 difference between modelled LST (from ORCHIDEE or H-TESSEL) and the EUMETSAT
23 LandSAF product (<http://landsaf.meteo.pt>).

24 *Spatial patterns*

25 The first EOF patterns of P and LST errors are represented in Fig. 7, together with their
26 explained variance. The precipitation error is common to both models as it originates in the
27 selected forcing. The dominant spatial structure of this error, which represents only 15% of
28 the total variance, has its maximum in the South-East of the IP and is different from the one
29 found for TB. The error patterns from LST differ remarkably between the two models and do
30 not seem related to the TB error. On the one hand, a North-South gradient is observed in
31 ORCHIDEE's LST error (Fig. 7 a), which is most likely explained by forcing induced biases

1 due to available energy affecting the LSM simulation. On the other hand, H-TESSEL's LST
2 error pattern (Fig. 7 c) shows a gradient from East to West.

3 *Expansion coefficients*

4 The ECs correspondent to each of these patterns are presented in Fig. 8. Those for the
5 precipitation error show a higher frequency variation than those of the LST and TB errors.
6 ORCHIDEE's LST error behaves as expected from land-surface physics, with a maximum in
7 summer when the largest amount of energy is absorbed by the surface and thus, small errors
8 in the energy balance translate into large temperature differences. This is not the case for H-
9 TESSEL's LST error, whose ECs show higher frequency variation with maxima in the fall
10 season and at the end of the winter in 2011 and 2012.

11 The dominant modes of variability of P and LST errors show different spatial and temporal
12 characteristics than the TB error dominant pattern. Neither the spatial structures coincide, nor
13 their temporal evolution over the 2010 to 2012 period. The TB errors show a strong annual
14 variation which peaks in fall and winter. The ECs of ORCHIDEE's LST error show a
15 maximum in summer, while those for H-TESSEL's LST and P errors are characterized by
16 higher frequency variations.

17 Therefore, this analysis excludes the hypothesis that biases in precipitation driving the models
18 or errors in their surface temperature are the direct cause of the inconsistency in TB's spatial
19 structures. The strong similarities of the TB errors in two quite different LSMs further
20 strengthens the rejection of this hypothesis.

21 **4.2.3 Analysis of CMEM assumptions**

22 The CMEM is another candidate to explain the TB error since it is also a common element
23 from both sets of modelled TBs. In fact, modelled TBs have been shown to be more sensitive
24 to the configuration of the microwave model than to the LSM used (de Rosnay et al., 2009).

25 As explained in section 2, we performed a sensitivity analysis to test if certain CMEM
26 parameterizations could explain the differences between measured and modelled TBs. As a
27 result, three new sets of modelled TBs were estimated: $TB_{HT(VC)}$, $TB_{OR(SD)}$, and $TB_{OR(FW)}$ to
28 evaluate the role of vegetation, vertical discretization, and the emissivity parameterization
29 respectively.

1 In the first place, $TB_{HT(VC)}$ shows similar mean spatial correlations with TB_{SM} as the ones for
2 TB_{HT} and TB_{SM} (Table 4). In addition, an EOF analysis of the difference between this new
3 estimate and observed TBs (figure not included) shows similar spatial patterns as the ones
4 identified in Fig. 4 (a and c), as well as a good agreement between their ECs.

5 In the second place, no significant differences were observed between $TB_{OR(SD)}$ and TB_{OR}
6 when compared to TB_{SM} . For instance, mean spatial correlations computed using $TB_{OR(SD)}$
7 and TB_{SM} are 0.22 and 0.33 for the horizontal and vertical polarization, which are similar to
8 the values obtained for TB_{OR} and TB_{SM} (Table 4).

9 In the third place, an EOF analysis of the TB error computed using the $TB_{OR(FW)}$ and the TB_{SM}
10 sets (figure not included), shows a similar dominant structure both in space and time to the
11 one observed in Fig. 3 (a and c). In addition, similar spatial correlations between $TB_{OR(FW)}$
12 and the TB_{SM} to those from TB_{OR} and TB_{SM} are also found (Table 4).

13 As synthesized in Table 4, in the current state of CMEM the vegetation cover, the number of
14 soil layers, and the ϵ_s and T_{eff} parameterizations can be discarded as the dominant factors
15 responsible for the poor spatial correlation between modelled and SMOS TBs.

16 **4.3 Annual cycle of TBs**

17 The slow varying component of the TB signals is analysed pixel by pixel, because it has been
18 identified as the driver of the largest spatially coherent error structure between measured and
19 modelled TBs (Fig. 5). For this matter, the mean annual cycle of each TB signal was
20 computed for each pixel and then smoothed using a spline filter to remove sub-monthly
21 fluctuations. The period of study is too short to ensure that a simple annual mean cycle filters
22 out high frequency variations. In Fig. 9 the normalized amplitudes of the annual TB cycle are
23 displayed.

24 The spatial structures shown in SMOS's maps (Fig. 9, c and f) exhibit strong resemblances to
25 those observed in the first EOF patterns of the TB error (Fig. 3 and 4, a and c). However, this
26 structure is not found in the maps corresponding to TB_{OR} and TB_{HT} , where there is less
27 contrast in the spatial distribution of the relative amplitude of the annual cycle. This indicates
28 that the LSMs combined with CMEM do not reproduce the annual cycle amplitude of TBs
29 observed by SMOS.

1 To further analyse this result, two study areas are defined (Fig.10). The first one is over the
2 South-Western IP (7.5W : 4W, 40N : 38N) and corresponds to part of the area where the
3 largest differences in TB's normalized amplitudes are identified. The second one is the North-
4 Western region (8.25W : 6W, 43N : 41.75N) of the IP and is chosen because it shows similar
5 annual cycle amplitudes of TB in the two models and SMOS. In addition, the EOF analysis of
6 the TB error showed opposite behaviours in these areas.

7 Fig. 10 shows the smoothed annual cycle of the horizontal and vertical polarizations of the TB
8 signals from both regions. The LST from the LandSAF product as well as those modelled by
9 ORCHIDEE and H-TESSEL are also displayed because of their direct relation to TBs. The
10 plots show that the TB's annual cycle behaviour differs between the two regions. Therefore,
11 the processes responsible for the TB error are probably different in each one of them.

12 The following results can be extracted from the plot corresponding to the South-Western area
13 (Fig. 10 a):

14 In winter the difference between models is small compared to their relative warm bias when
15 compared to SMOS. In summer the agreement is relatively good with observations laying
16 within the spread of the models. This explains the result presented above, namely that the
17 amplitude of the simulated annual cycle is smaller than for the remotely sensed TB.
18 Examining the LST one can note that the biases are relatively small and ORCHIDEE
19 generally matches better the LandSAF product, but H-TESSEL shows a larger and more
20 correct amplitude of the annual cycle. This might explain why this model has the largest
21 amplitude of TB in both polarisations, indicating that a large fraction of the error on the
22 annual cycle of TB is caused by the emissivity simulated by CMEM given the surface states
23 of both LSMs.

24 Over the North-Western IP SMOS observations are mostly within the uncertainty spanned by
25 the two models. One notable exception is the summer period for the horizontal polarization
26 where both models are cooler. Also in this region the amplitude of TB in both polarizations is
27 larger in H-TESSEL than ORCHIDEE and closer to that measured by SMOS. Again, this can
28 be related to LST. Although ORCHIDEE has smaller biases, the H-TESSEL amplitude of the
29 annual cycle is larger and closer to the observed one.

30 The strong difference in behaviour between the two selected regions in winter explains the
31 resemblance of the dominant EOF mode in TB errors of both models with the regions of
32 maximum amplitude of the annual cycle of observed TBs. For both regions, the LST biases of

1 the LSMs do not show a clear relation to the simulated TBs. H-TESEL has the warmest
2 surface temperatures but the lowest TBs, indicating that its state variables produce a lower
3 emissivity than ORCHIDEE when processed by CMEM. On the other hand the differences in
4 annual amplitudes of LST could contribute to those seen for the TB. This is also supported by
5 the fact that the dominant variation modes of LST errors are not related to those of TBs. This
6 would indicate that the major contribution to the TB errors found for the models does not
7 originate in their forcing or their ability to simulate the land surface energy balance and
8 temperature, but rather in the way CMEM simulates L-band emissivity based on their
9 description of the surface state.

10 **5 Discussion**

11 This work complements with an analysis of TBs the study by Polcher et al. (2015), which
12 compared the SSM product of SMOS with ORCHIDEE's modelled SSM. Both studies
13 present a spatio-temporal correlation analysis and obtain similar results: a good agreement in
14 temporal evolutions and a large mismatch between the spatial structures of measured and
15 modelled SSM and TB.

16 The temporal correlation between TB_{OR} and TB_{SM} is very similar to that between retrieved
17 (SMOS) and modelled (ORCHIDEE) SSM (Table 4). In addition, both variables show lower
18 correlations over mountain ranges. As noted for SSM, the temporal correlation is mainly
19 driven by its fast varying component and is not very sensitive to the annual cycle (Polcher et
20 al., 2015).

21 Spatial correlations are low for both variables, indicating an inconsistency between the spatial
22 structures of measured and modelled data. Polcher et al. (2015) showed that the spatial
23 correlation between retrieved and modelled SSM is worse for the SSM's slow varying
24 component than for its fast varying component. This can be due to the fact that the largest
25 spatially coherent error between measured and modelled TBs is dominated by their slow
26 varying component, as shown in this paper.

27 The EOF analysis presented here identified a dominant structure over the South-Western IP
28 using both sets of modelled TBs, which explains a large fraction of the TB error. This
29 structure differs from the error characterization of the SSM comparison, which showed the
30 largest discrepancies between modelled and retrieved SSM over the North-Western IP. In
31 fact, only weak differences were found for SSM over the South-Western region (Polcher et
32 al., 2015). These results indicate that the transfer functions used by SMOS to derive SSM

1 from observed TBs or CMEM, which estimates TBs from modelled SSM (together with other
2 state variables), play an important role and have to be better understood in order to explain the
3 differences between the SMOS observations and the simulated surface states.

4 None of the hypotheses tested to identify a methodological weakness in the forcing of both
5 LSMs or the configuration of CMEM, which would explain this common error, was
6 conclusive. The differences in TB between the LSMs and SMOS are noteworthy and we
7 believe that understanding them should be a priority for the community to achieve a better
8 usage of these observations. As the LSMs used here are very different in their conception, it is
9 unlikely that they produce the same systematic SSM bias which would explain the large
10 discrepancy in the South-West of the IP during winter. On the other hand, processes which
11 are not represented with enough detail in both schemes could explain the error and need to be
12 analysed as to their potential to explain the discrepancies.

- 13 • In the first place, it is interesting to study the Leaf Area Index (LAI), because it is
14 linked to the seasonal cycle of vegetation. It may, therefore, reveal some
15 underestimated effects of vegetation dynamics on modelled TBs, which could be
16 related, to a certain extent, to the seasonality identified in the dominant structure of the
17 TB error. In addition, the LAI is a key component in the CMEM parameterization of
18 τ_{veg} . However, the areas of the IP where the TB error is the largest are those of least
19 vegetation. Therefore, in our opinion, modelled LAI is not likely to be the main cause
20 of the differences in TB's spatial structures.
- 21 • In second place, assumptions made in the modelling of rainfall interception may also
22 explain some differences between modelled and measured TBs. In particular, those
23 shown in Fig. 10 (b) over the North-Western region of the IP. This region is
24 characterized by an oceanic climate and thus, wet winters and mild summers, with a
25 high precipitation, and often rainfall occurring as drizzle. Contrary to the Southern
26 region, there is more vegetation and thus, rainfall interception plays a key role over
27 this area and may be of interest to revise how this process is modelled. However, the
28 IP region with strong interception is not the one with the largest TB error. The error
29 over the South-Western region is larger than over the North-Western region, as shown
30 by the EOF analysis.
- 31 • In third place, the attenuation effect of litter on the soil and its interception of water
32 could also explain differences obtained between modelled and measured TBs, since it

1 is not taken into account by models, but is part of satellite observations. However, we
2 believe that probably it would not cause an impact structured as the one observed over
3 the South-Western area of the IP without affecting other regions. Indeed this process
4 would be strongest in regions with dense vegetation.

5 • Finally, issues related to the fundamental simplification of subgrid processes in LSMs
6 may also contribute to the inconsistency between the spatial structures of modelled
7 and measured TBs. For instance, LSMs do not represent small scale features as open
8 water in lakes and rivers, swamps, irrigated areas or other water ponded on the surface
9 and could contribute strongly to L-band emissivity of the surface. Assumptions made
10 by LSMs could neglect key issues from the small scale which could be carried over to
11 the large scale of TBs. For the moment, we do not see why these simplifications of
12 LSMs would have the strongest impact in the South-West of the IP.

13 Instrumental issues from SMOS could also explain the differences in TB spatial structures, in
14 case these are not of climatological or geophysical nature. For example, one of the most
15 important causes of noise in SMOS surface soil moisture is Radio-Frequency Interferences
16 (RFIs). Daganzo-Eusebio et al. (2013) describe their effect on SMOS data. Some of them are
17 difficult to detect and thus, RFIs may not be properly filtered out. For instance, Dente et al.
18 (2012) identified an irregular angular pattern in the TBs affecting data from the L1C product
19 used to retrieve soil moisture. In their opinion, this was caused by weak RFIs which were not
20 correctly filtered. Another explanation could be antenna pattern errors, as SMOS TBs
21 seasonal and latitudinal drifts detailed in Oliva et al. (2013). However, RFIs are not likely to
22 be the main cause of the differences between measured and modelled TBs, because the main
23 spatial structure identified in both TB errors is found to be dominated by the brightness
24 temperature's annual cycle. This suggests that it contains a geophysical signal.

25 In our opinion, further analyses should be carried out regarding the CMEM assumptions
26 concerning emissivity. According to Jones et al. (2004), the soil moisture and vegetation
27 water content have a significant effect on the sensitivity of TB at the top of the atmosphere.
28 However, they impact microwave emission in different ways. On the one hand, an increase in
29 soil moisture results in a higher soil dielectric constant (ϵ) and thus, on lower emissivities. On
30 the other hand, an increase in the vegetation water content rises the scatter and the absorption,
31 increasing the emission. The ϵ is key in the computation of emissivity, while the vegetation
32 optical depth (τ_{veg}) is closely related to the vegetation water content. Both variables are

1 modelled in CMEM and the same parameterization has been used to estimate the two sets of
2 modelled TBs: Wang and Schmugge (1980) for ϵ and Wigneron et al. (2007) for τ_{veg} .
3 Furthermore, the same parameterization has been used to model the rough surface emissivity
4 (ϵ_r) in both cases: Wigneron et al., 2001. Considering that similar spatial patterns were
5 obtained for the TB error using two different LSMs, focus should be put on the above
6 mentioned variables (ϵ , τ_{veg} , and ϵ_r) in CMEM. We suggest to prioritize the analysis of the
7 relation between the vegetation water content and TB because of the role the vegetation
8 opacity model plays in CMEM's configuration, as shown in de Rosnay et al. (2009). In
9 addition, no significant differences were observed between modelled and retrieved SSM over
10 South-Western IP (Polcher et al. 2015), where the maximum TB error was identified. This
11 reassures our suggestion of prioritizing τ_{veg} with respect to ϵ , since the latter is directly related
12 to SSM.

13 **6 Conclusions**

14 TBs of SMOS Level 1C product were compared to two sets of modelled TBs. The latter were
15 obtained using simulated state variables (from the ORCHIDEE and H-TESSEL LSMs) and a
16 radiative transfer model, CMEM. The study was carried out over the Iberian Peninsula (IP)
17 for the period 2010 to 2012.

18 On the one hand, a temporal correlation analysis between measured and modelled data shows
19 that there is a good agreement in their temporal evolution. However, this diagnostic is mainly
20 driven by the TB's signal synoptic variability, as occurs with SSM (Polcher et al., 2015). On
21 the other hand, a spatial correlation analysis detected a large mismatch between the TB spatial
22 structures provided by models and observations.

23 An EOF analysis of the error between modelled and measured TBs suggests that the
24 inconsistency is not limited to a particular LSM. It is dominated by the TB slow varying
25 component, peaking in fall and winter. In addition, modelled TBs are larger than SMOS
26 measurements during these seasons over the dominant error structure detected. This structure
27 explains between 18% and 36% of the TB error variance, depending on the LSM and
28 polarization. Therefore, there is a high percentage of the error (between 82% and 64%) that
29 shows structures which have to be analysed and explained. Since these are not present in both
30 LSMs, they are of lower priority and have not been approached in this study.

31 Forcing induced biases are discarded as the main cause of the spatial inconsistency in TBs
32 after computing the dominant error structures of precipitation and Land Surface Temperature

1 (LST). Nevertheless, the degree of accuracy of the forcing cannot be fully established because
2 of scale issues and the lack of sufficient independent measurements. The difference in TBs'
3 spatial structures could also be thought of a combination of non linear relations between
4 errors in precipitation and LST, but this is beyond the scope of this paper.

5 Assumptions made in certain CMEM parameterizations are also discarded as the main source
6 of the spatial inconsistency between measured and modelled TBs: the vegetation cover input;
7 the number of soil layers defined; and some parameterizations to compute the smooth surface
8 emissivity (Fresnel law and Wilheit (1978)) and the effective temperature (Wigneron et al.
9 (2001) and the temperature profile).

10 Previous studies found differences between the spatial structures of modelled and retrieved
11 SSM (Parrens et al., 2012; Polcher et al., 2015). This paper shows that these structures are not
12 consistent also when comparing modelled and observed TBs. In addition, this issue is
13 amplified for the TBs compared to SSM, because the latter are bounded by zero and
14 saturation. This could explain the generally better spatial correlation for SSM in winter, when
15 it reaches saturation in large parts of the IP. Although this study is limited to the IP,
16 differences in spatial structures occur at a global scale. We would like to draw the reader's
17 attention to the fact that TBs are not only the main input of SMOS soil moisture retrieval
18 algorithm, but that they are used to retrieve other variables, like vegetation optical depth or
19 salinity. We believe that analysing the spatial inconsistencies between modelled and measured
20 TBs is important, as these can affect the estimation of geophysical variables, TB assimilation
21 in operational models, as well as result in misleading validation studies. Therefore, obtaining
22 the spatial contrast of measured TBs in models is a challenge which, in our opinion, deserves
23 a higher priority in the community.

24 **Acknowledgements**

25 The authors would like to thank Filipe Aires and Jean-Pierre Wigneron for their helpful
26 comments. This work contributes to the FP7 Earth2Observe project under grant agreement No
27 603608.

28

1 **References**

2 Albergel, C., Zakharova, E., Calvet, J. C., Zribi, M., Pardé, M., Wigneron, J. P., Novello, N.,
3 Kerr, Y., Mialon, A., and Fritz, N.: A first assessment of the SMOS data in southwestern
4 France using in situ and airborne soil moisture estimates: The CAROLS airborne campaign,
5 Remote Sens. Environ., vol. 115, no. 10, pp. 2718–2728, 2011.

6 Balsamo, G., Vitterbo, P., Beljaars, A., van den Hurk, B., Hirschi, M., Betts, A. K., and
7 Scipal, K.: A Revised Hydrology for the ECMWF Model: Verification from Field Site to
8 Terrestrial Water Storage and Impact in the Integrated Forecast System, J. Hydrometeor., 10,
9 623-643, DOI:10.1175/2008JHM1068.1, 2009.

10 Baroni G., Facchi A., Gandolfi C., and Ortuan B.: Analysis of the performances of methods
11 for the evaluation of soil hydraulic parameters and of their application in two hydrological
12 models. In : Santini A. (ed.), Lamaddalena N. (ed.), Severino G. (ed.), Palladino M. (ed.).
13 Irrigation in Mediterranean agriculture: challenges and innovation for the next decades. Bari :
14 CIHEAM, 213- 222 (Options Méditerranéennes : Série A. Séminaires Méditerranéens; n. 84) ,
15 2008.

16 Bircher, S. and Kerr, Y.: Validation of SMOS L1C and L2 Products and Important Parameters
17 of the Retrieval Algorithm in the Skjern River Catchment, Western Denmark, IEEE Trans.
18 Geosc. Rem. Sens., 51, 5, 2013.

19 Björnsson, H., and Venegas, S. A.: A Manual for EOF and SVD Analyses of Climate Data.
20 Report No 97-1, Department of Atmospheric and Oceanic Sciences and Centre for Climate
21 and Global Change Research, McGill University, 52, 1997.

22 Bousseta, S., Balsamo, G., Beljaars, A., Kral, T., and Jarlan, L.: Impact of a satellite-derived
23 leaf area index monthly climatology in a global numerical weather prediction model.
24 International Journal of Remote Sensing 34, 9-10, 3520-3542,
25 <http://dx.doi.org/10.1080/01431161.2012.716543>, 2013.

26 Cayan, D. R. and Georgakakos, K. P.: Hydroclimatology of continental watersheds. 2. Spatial
27 analyses. Water Resources Research 31: doi: 10.1029/94WR02376. Issn: 0043-1397, 1995.

28 Daganzo-Eusebio, E., Oliva, R., Kerr, Y., Nieto, S., Richaume, P., and Mecklenburg, S.:
29 SMOS radiometer in the 1400-1427-MHz passive band: Impact of the RFI environment and

1 approach to its mitigation and cancellation, IEEE Trans. Geosci. Remote Sens., vol. 51, no.
2 10, pp. 4999–5007, 2013.

3 De Rosnay, P. and Polcher, J.: Improvements of the Representation of the Hydrological
4 Exchanges between the Biosphere and the Atmosphere in a GCM, Hydrology and Earth
5 System Sciences 2 (2-3): 239–56, 1998.

6 De Rosnay P., Drusch, M., Boone, A., Balsamo, G., Decharme, B., Harris, P., Kerr, Y.,
7 Pellarin, T., Polcher, J., and Wigneron, J. P.: The AMMA Land Surface Model
8 Intercomparison Experiment coupled to the Community Microwave Emission Model:
9 ALMIP-MEM", J. Geophys. Res., Vol 114, doi: 10.1029/2008JD010724, 2009.

10 Dee, D. P., Uppala, S. M., Simmons, A. J., Berrisford, P., Poli, P., Kobayashi, S., Andrae, U.:
11 The ERA-Interim Reanalysis: Configuration and Performance of the Data Assimilation
12 System, Quarterly Journal of the Royal Meteorological Society 137 (656): 553–97.
13 doi:10.1002/qj.828, 2011.

14 Dente. L., Su, Z., and Wen, J.: Validation of SMOS Soil Moisture Products over the Maqu
15 and Twente Regions. Sensors, 12, 9965-9986, doi:10.3390/s120809965, 2012.

16 D'Orgeval, T., Polcher, J., and de Rosnay, P.: Sensitivity of the West African hydrological
17 cycle in ORCHIDEE to in- filtration processes, Hydrol. Earth Syst. Sci., 12, 1387–1401,
18 doi:10.5194/hess-12-1387-2008, 2008.

19 Drusch, M., Wood, and Jackson, T.: Vegetative and atmospheric corrections for soil moisture
20 retrieval from passive microwave remote sensing data: Results from the Southern Great Plains
21 Hydrology Experiment 1997, J. Hydromet., 2, 181-192, 2001.

22 Entekhabi, D., Njoku, E. G., O'Neill, P. E., Kellogg, K. H., Crow, W. T., Edelstein, W. N.,
23 Entin, J. K., Goodman, S. D., Jackson, T. J., Johnson, J., Kimball, J., Piepmeier, J. R., Koster,
24 R. D., Martin, N., McDonald, K. C., Moghaddam, M., Moran, S., Reichle, R., Shi, J. C.,
25 Spencer, M. W., Thurman, S. W., Tsang, L., and Van Zyl, J.: The Soil Moisture Active
26 Passive (SMAP) Mission, Proceedings of the IEEE 98.5, 704-716, 2010.

27 Escorihuela, M. J., Chanzy, A., Wigneron, J. P., and Kerr. Y.: Effective Soil Moisture
28 Sampling Depth of L-Band Radiometry: A Case Study. Remote Sensing of Environment 114
29 (5): 995–1001. doi:10.1016/j.rse.2009.12.011, 2010.

1 González-Zamora, A., Sánchez, N., Gumuzzio, A., Piles, M., Olmedo, E., and Martínez-
2 Fernández, J.: Validation of SMOS L2 and L3 soil moisture products over the Duero Basin at
3 different spatial scales. *The International Archives of Photogrammetry, Remote Sensing and*
4 *Spatial Information Sciences*, XL-7/W3, 2015.

5 Green, W. H. and Ampt, G.: Studies on soil physics, 1. the flow of air and water through soils.
6 *J. Agric. Sci*, 4(1) :1–24, 1911.

7 Haylock, M. R., Hofstra, N., Klein Tank, A. M. G., Klok, E. J., Jones, P. D., and New, M.: A
8 European daily high-resolution gridded dataset of surface temperature and precipitation. *J.*
9 *Geophys. Res (Atmospheres)*, 113, D20119, doi:10.1029/2008JD10201, 2008.

10 Holmes, T. R. H., Jackson, T. J., Reichle, R. H., Basara, J .B.: An assessment of surface soil
11 temperature products from numerical weather prediction models using ground-based
12 measurements, *Water Resources Research*, 48 (2), p. W02531
13 <http://dx.doi.org/10.1029/2011WR010538>, 2012.

14 Hourdin, F.: Etude et simulation numérique de la circulation générale des atmosphères
15 planétaires, PhD Thesis, available at: www.lmd.jussieu.fr/~hourdin/these.pdf, 1992.

16 Jones, A., Vukićević, T., and Vonder Haar, T.: A microwave satellite observational operator
17 for variational data assimilation of soil moisture, *J. Hydrometeor.*, 5, 213– 229, 2004.

18 Kanamitsu, M., Yoshimura, K., Yhang, Y. B., and Hong, S. Y.: Errors of Interannual
19 Variability and Trend in Dynamical Downscaling of Reanalysis, *J. Geophys. Res.*, 115,
20 17115, doi:10.1029/2009JDO13511, 2010.

21 Kerr, Y., Waldteufel, P., Wigneron, J. P., Delwart, S., Cabot, F., Boutin, J., Escorihuela, M.,
22 Font, J., Reul, N., Gruhier, C., Juglea, S., Drinkwater, M., Hahne, A., Martin-Neira, M., and
23 Mecklenburg, S.: The SMOS mission: New tool for monitoring key elements of the global
24 water cycle, *Proc. IEEE*, 98, 5, 666-687, 2010.

25 Kerr, Y., Waldteufel, P., Richaume, P., Wigneron, J. P., Ferrazzoli, P., Mahmoodi, A., Bitar,
26 A. A., Cabot, F., Gruhier, C., Juglea, S., Leroux, D., Mialon, A., and Delwart, S.: The SMOS
27 soil moisture retrieval algorithm, *IEEE Trans. Geosci. Remote Sens*, 50, 5, 1384-1403, 2012.

28 Kolassa, J., Aires. F., Polcher, J., Pringent, C., Jiménez, C., and Pereira, J. M.: Soil
29 moisture retrieval from multi-instrument observations: Information content analysis and

1 retrieval methodology, J. Geophys. Res. Atmos., 118, 4847–4859,
2 doi:10.1029/2012JD018150, 2013.

3 Krinner, G., N. Viovy, N., de Noblet-Ducoudré, N., Ogée, J., Polcher, J., Friedlingstein, P.,
4 Ciais, P., Stich, S., and I. C Prentice. 2005.: A Dynamic Global Vegetation Model for Studies
5 of the Coupled Atmosphere-Biosphere System. *Global Biogeochemical Cycles* 19 (1).
6 doi:10.1029/2003GB002199, 2005.

7 Le Vine, D., Lagerloef, G. S. E., and Torrusio, S.: Aquarius and remote sensing of sea surface
8 salinity from space, P. IEEE , 98, 688–703, doi:10.1109/JPROC.2010.2040550, 2010.

9 Marthews, T. R., Quesada, C. A., Galbraith, D. R., Malhi, Y., Mullins, C. E., Hodnett, M. G.,
10 and Dharssi, I.: High-resolution hydraulic parameter maps for surface soils in tropical South
11 America, *Geosci. Model Dev.*, 7, 711-723, doi:10.5194/gmd-7-711-2014, 2014.

12 Mätzler, C., and Standley, A.: Technical Note: Relief Effects for Passive Microwave Remote
13 Sensing. *International Journal of Remote Sensing* 21 (12): 2403–12,
14 doi:10.1080/01431160050030538, 2000.

15 McMullan K., Brown, M., Martín-Neira, M., Rits, W., Ekholm, S., Marti, J., and
16 Lemanczyck, J.: “SMOS: The payload”, *IEEE Trans. Geosci. Remote Sens.*, 46, 3, 594–605,
17 2008.

18 Milly, P. C. D.: Potential evaporation and soil moisture in general circulation models, *J. Climate*, 5, 209–226, 1992.

20 Montzka, C., Bogena, H., Weihermüller, L., Jonard, F., Dimitrov, M., Bouzinac, C.,
21 Kainulainen, J., Balling, J. E., Vanderborght, J., and Vereecken, H.: Radiobrightness
22 validation on different spatial scales during the SMOS validation campaign 2010 in the Rur
23 catchment, Germany, *IEEE Transactions on Geoscience and Remote Sensing*, 51, 1728-1743,
24 doi:10.1109/TGRS.2012.2206031, 2013.

25 Ngo-Duc, T., Polcher, J., and Laval, K.: A 53-Year Forcing Data Set for Land Surface
26 Models, *Journal of Geophysical Research* 110 (D6). doi:10.1029/2004JD005434, 2005.

27 Oliva, R., Martín-Neira, M., Corbella, I., Torres, F., Kainulainen, J., Tenerelli, J., Cabot, F.,
28 and Martin-Porqueras, F.: SMOS calibration and instrument performance after one year in
29 orbit, *IEEE Trans. Geosci. Remote Sens.*, vol. 51, no. 1, pp. 654–670, 2013.

1 Parrens, M., Zakharova, E., Lafont, S., Calvet, J.-C., Kerr, Y., Wagner, W., and Wigneron, J.-
2 P.: Comparing Soil Moisture Retrievals from SMOS and ASCAT over France, *Hydrology and*
3 *Earth System Sciences* 16 (2): 423–40. doi:10.5194/hess-16-423-2012, 2012.

4 Parrens, M., Calvet, J.-C., de Rosnay, P., and Decharme, B.: Benchmarking of L-band soil
5 microwave emission models, *Remote Sensing of Environment*, 140 pp 407-419, doi:
6 10.1016/j.rse.2013.09.017, 2014.

7 Pellarin, T., Wigneron, J. P., Calvet, J.-C., and Waldteufel, P.: Global soil moisture retrieval
8 from a synthetic L-band brightness temperature data set, *Journal of Geophysical Research*
9 (*Atmospheres*), 108, 4364, doi:10.1029/2002JD003086, 2003.

10 Polcher, J., Piles, M., Gelati, E., Tello, M., and Barella-Ortiz, A.: Comparing Upper-Soil
11 moisture from SMOS and a land-surface model over the Iberian Peninsula, Accepted.

12 Post, W. M., and Zobler, L.: Global Soil Types, 0.5-Degree Grid (Modified Zobler).
13 Available on-line [<http://www.daac.ornl.gov>] from Oak Ridge National Laboratory
14 Distributed Active Archive Center, Oak Ridge, Tennessee, U.S.A., 2000

15 Rüdiger, C., Walker, J. P., Yann, K., Mialon, A., Merlin, O., and Kim, E. J.: Validation of the
16 level 1c and level 2 SMOS products with airborne and ground-based observations, *Proc. Int.*
17 *Congr. MODSIM*, Perth, Australia, Dec. 12-16, 2011.

18 Sánchez, N., Martínez-Fernández, J., Scaini, A., and Pérez-Gutiérrez, C.: Validation of the
19 SMOS L2 Soil Moisture Data in the REMEDHUS Network (Spain). *IEEE Transactions on*
20 *Geoscience and Remote Sensing* 50 (5): 1602–11, doi:10.1109/TGRS.2012.2186971, 2012.

21 Santaren D., Peylin P., Viovy N., Ciais P. : Optimizing a process-based ecosystem model with
22 eddy-covariance flux measurements: a pine forest in southern France, *Global Biogeochem.*
23 *Cycles*, 21, p. GB2013, 2007.

24 Schlenz, F., dall'Amico, T., Mauser, W., and Loew, A.: Analysis of SMOS brightness
25 temperature and vegetation optical depth data with coupled land surface and radiative transfer
26 models in Southern Germany, *Hydrol. Earth Syst. Sci. Discuss.*, 9, 4, 5389-5436, 2012.

27 Schulz, J. P., Dümenil, L., and Polcher, J.: On the Land Surface–Atmosphere Coupling and
28 Its Impact in a Single-Column Atmospheric Model, *Journal of Applied Meteorology* 40, 642-
29 663, 2001.

1 Ulaby, F. T., Moore, R. K., and Fung, A. K.: Microwave Remote Sensing (Active and
2 Passive), vol. 2. Reading, MA: Addison-Wesley, 1986.

3 Viterbo, P. and Beljaars, A.: An improved land surface parameterization scheme in the
4 ECMWF model and its validation. *Journal Climate*, vol. 8, pp. 2716-2748, 1995.

5 Wang, F., Cheruy, F., and Dufresne, J.-L.: The improvement of soil thermodynamics and its
6 effects on land surface meteorology in the IPSL climate model. *Geosci. Model Dev.*, 9, 363–
7 381, doi:10.5194/gmd-9-363-2016, 2016.

8 Wang, J. R., and Schmugge, T.: An empirical model for the complex dielectric permittivity of
9 soils as a function of water content, *IEE Trans. Geosc. Remote Sens.*, 18, 288-295, 1980.

10 Wigneron, J. P., Laguerre, L., and Kerr, H.: A Simple Parameterization of the L-band
11 Microwave Emission from Rough Agricultural Soils, *IEEE Trans. Geos. Remot. Sens.*, 39,
12 1697-1707, 2001.

13 Wigneron, J. P., Kerr, Y., Waldteufel, P., Saleh, K., Escorihuela, M., Richaume, P.,
14 Ferrazzoli, P., Grant, J. P., Hornbuckle, B., de Rosnay, P., Calvet, J.-C., Pellarin, T., Gurney,
15 R., and Mätzler, C.: L-band microwave emission of the biosphere (L-MEB) model: Results
16 from calibration against experimental data sets over crop fields, *Remote Sens. Environ.*, 107,
17 4, 639–655, 2007.

18 Wilheit, T. T.: Radiative transfert in plane stratified dielectric, *IEEE Trans. Geos. Remot.*
19 *Sens.*, 16, 2, 138-143, 1978.

20 WWAP (World Water Assessment Programme): The United Nations World Water
21 Development Report 4: Managing Water under Uncertainty and Risk, Paris, UNESCO, 2012.

22 Zollina, O., Kapala, A., Simmer, C., and Gulev, S. K.: Analysis of extreme precipitation over
23 Europe from different reanalyses: a comparative assessment. *Global and Planetary Change* 44
24 129-161, 2004.

25

1 Table 1. CMEM configuration for the two sets of modelled TBs.

	Configuration	Parameterization	
		ORCHIDEE	H-TESSEL
Physical configuration	Soil dielectric constant	Wang and Schmugge (1980)	
	Effective temperature	Soil temperature profile	Wigneron et al. (2001)
	Smooth surface emissivity	Wilheit (1978)	Fresnel law
	Rough surface emissivity	Wigneron et al. (2001)	
	Vegetation optical depth	Wigneron et al. (2007)	
	Atmospheric optical depth	Pellarin et al. (2003)	
	Temperature of vegetation	Surface soil temperature	
	Vegetation cover input data	Ecoclimap	
Observing configuration	Microwave frequency	1.4Ghz	
	Incidence angle	42.5°	40°
Soil and atmospheric level configuration	Number of soil layers* (number of layers in the top 5 cm)	11 (5)	3 (1)

2 *Layer depths of ORCHIDEE's hydrological scheme [cm]: 0.099, 0.391, 0.978, 2.151, 4.497,
3 9.189, 18.570, 37.340, 74.880, 150, and 200

4 *Layer depths of H-TESSEL's hydrological scheme [cm]: 7, 21, 72, and 189

5

6

7

8

9

10

11

12

13

14

1
2

3 Table 2: Input variables for the CMEM to compute TBs at TOA.

Soil conditions	Constant fields	Soil texture fraction [%]
		Orography [km]
Vegetation	Constant fields	High and low vegetation types
		High and low vegetation fractions
		Water fraction
	Dynamic fields	Low vegetation LAI
Meteorology	Dynamic fields	Soil moisture profile [m^3m^{-3}]
		Soil temperature profile [K]
		Skin temperature [K]
		Snow depth [m]
		Snow density [kgm^{-3}]
		2 m temperature [K]

4
5
6
7
8
9
10

1
2

3 Table 3: TB filtering criteria to keep data, applied to the TB signals.

TB _{OR}	TB _{HT}	All TB signals
ORCHIDEE's daily average surface temperature > 275 K	Snow water equivalent < 0.01 m	Daily TB < 300 K
ERA-Interim's daily average 2 m air temperature > 273 K	ERA-Interim's daily average 2 m air temperature > 273.5K Orography (slope) < 0.04	Mask (from SMOS's L2 product)

4
5
6
7
8
9
10
11
12
13
14
15
16
17
18
19

1
2

3 Table 4: Mean temporal and spatial correlations for SSM (Polcher et al., accepted) and the
4 horizontal and vertical polarization of TBs over the Iberian Peninsula from 2010 to 2012.

	Temporal		Spatial	
	Horizontal	Vertical	Horizontal	Vertical
TB _{OR} vs. TB _{SM}	0.75	0.76	0.20	0.30
TB _{HT} vs. TB _{SM}	0.82	0.82	0.24	0.29
TB _{HT(VC)} vs. TB _{SM}	-	-	0.17	0.36
TB _{OR(SD)} vs. TB _{SM}	-	-	0.22	0.33
TB _{OR(FW)} vs. TB _{SM}	-	-	0.20	0.30
SSM _{OR} vs. SSM _{SM}	0.81		0.28	

5
6
7
8
9
10
11
12
13
14
15
16
17
18
19
20

1
2
3
4
5 Table 5: Spatial correlation for the first and second variation modes of the EOF analyses
6 performed for the difference between modelled and measured TBs. TBH and TBV correspond
7 to the horizontal and vertical polarizations, respectively.

	Mode 1	Mode 2
$TB_{OR} - TB_{SM}$ (TBH) vs. $TB_{OR} - TB_{SM}$ (TBV)	0.99	0.97
$TB_{HT} - TB_{SM}$ (TBH) vs. $TB_{HT} - TB_{SM}$ (TBV)	0.86	0.75
$TB_{OR} - TB_{SM}$ (TBH) vs. $TB_{HT} - TB_{SM}$ (TBH)	0.92	0.69
$TB_{OR} - TB_{SM}$ (TBV) vs. $TB_{HT} - TB_{SM}$ (TBV)	0.73	0.48

8
9
10
11
12
13
14
15
16
17
18
19
20

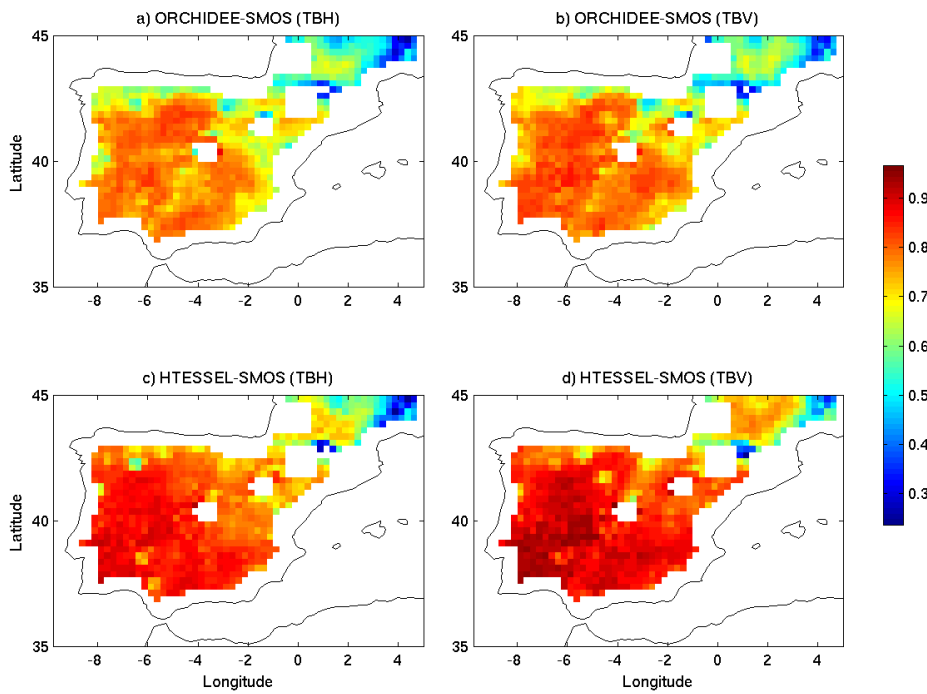
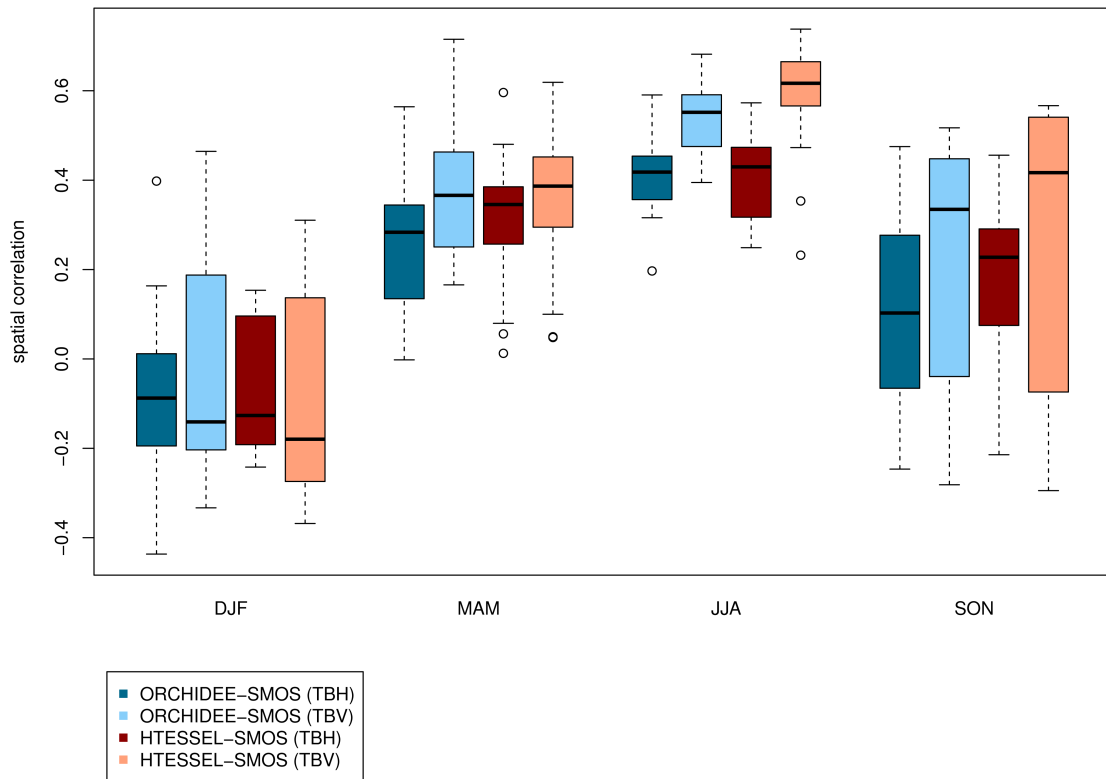


Figure 1: Temporal correlation between modelled and measured TBs from 2010 to 2012. TBH and TBV correspond to the horizontal and vertical polarizations, respectively.

1
2

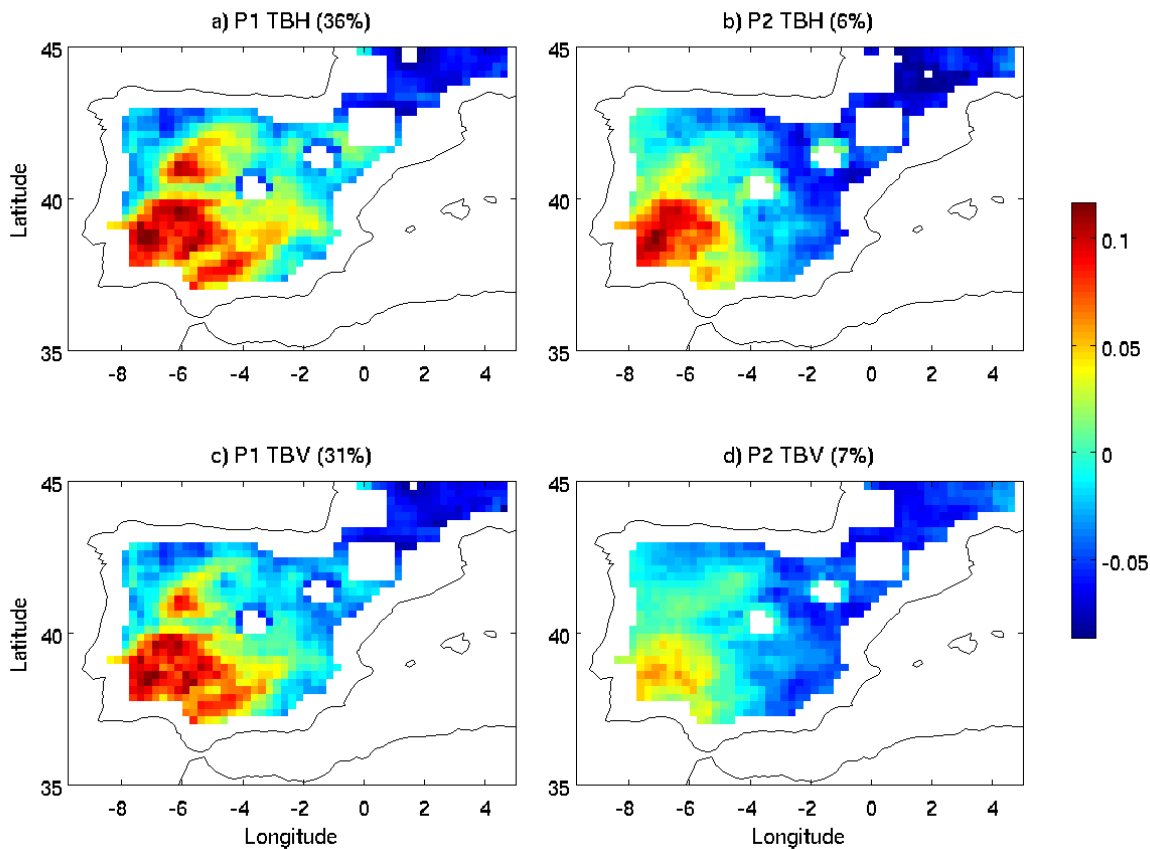


3

Figure 2: Boxplot showing the annual cycle of the spatial correlation between modelled and measured TBs, over the Iberian Peninsula from 2010 to 2012. TBH and TBV correspond to the horizontal and vertical polarizations, respectively. Values have been grouped per seasons: winter (DJF), spring (MAM), summer (JJA), and fall (SON).

8
9
10
11
12
13
14

1
2



3
4 Figure 3: Spatial patterns associated with the first two EOF variation modes (P1 and P2) of
5 the difference between modelled TB (ORCHIDEE) and measured TB (SMOS). TBH and
6 TBV correspond to the horizontal and vertical polarizations, respectively. The percentage of
7 variance explained by each mode is included in brackets.

8
9
10
11
12
13
14

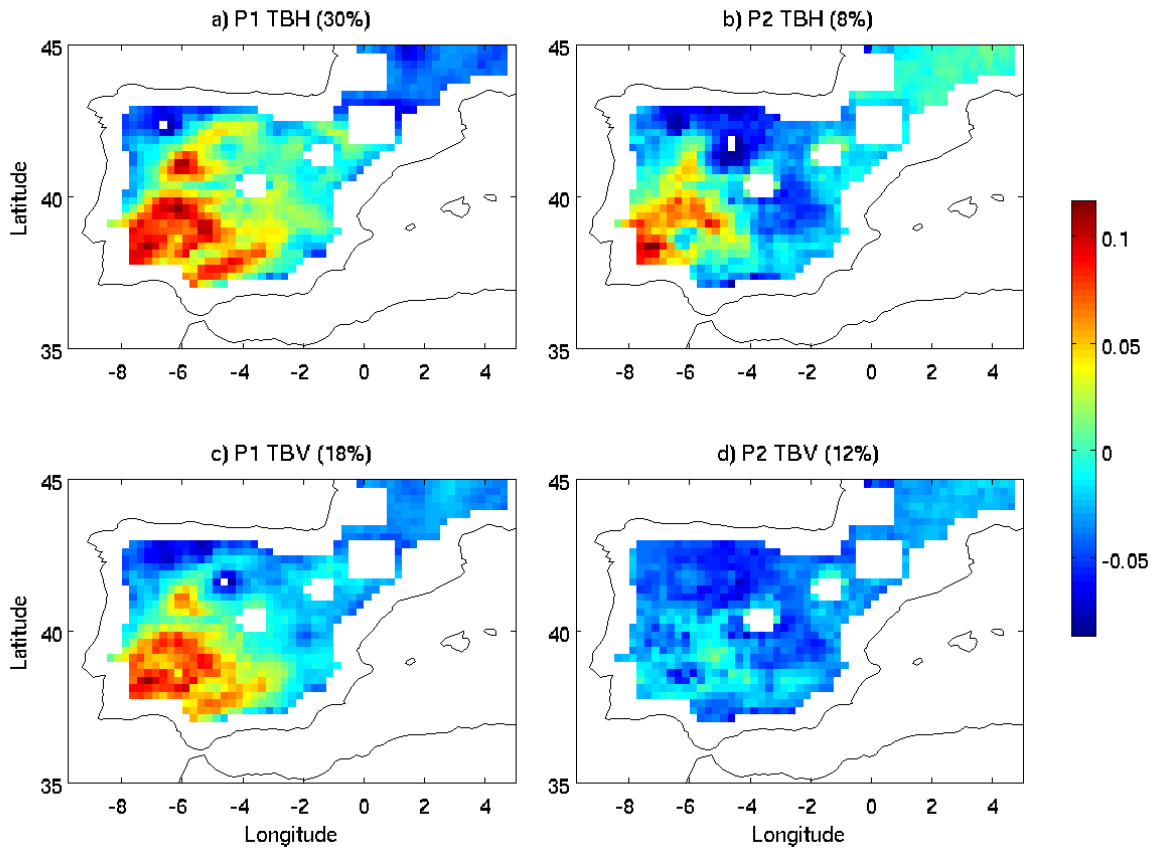
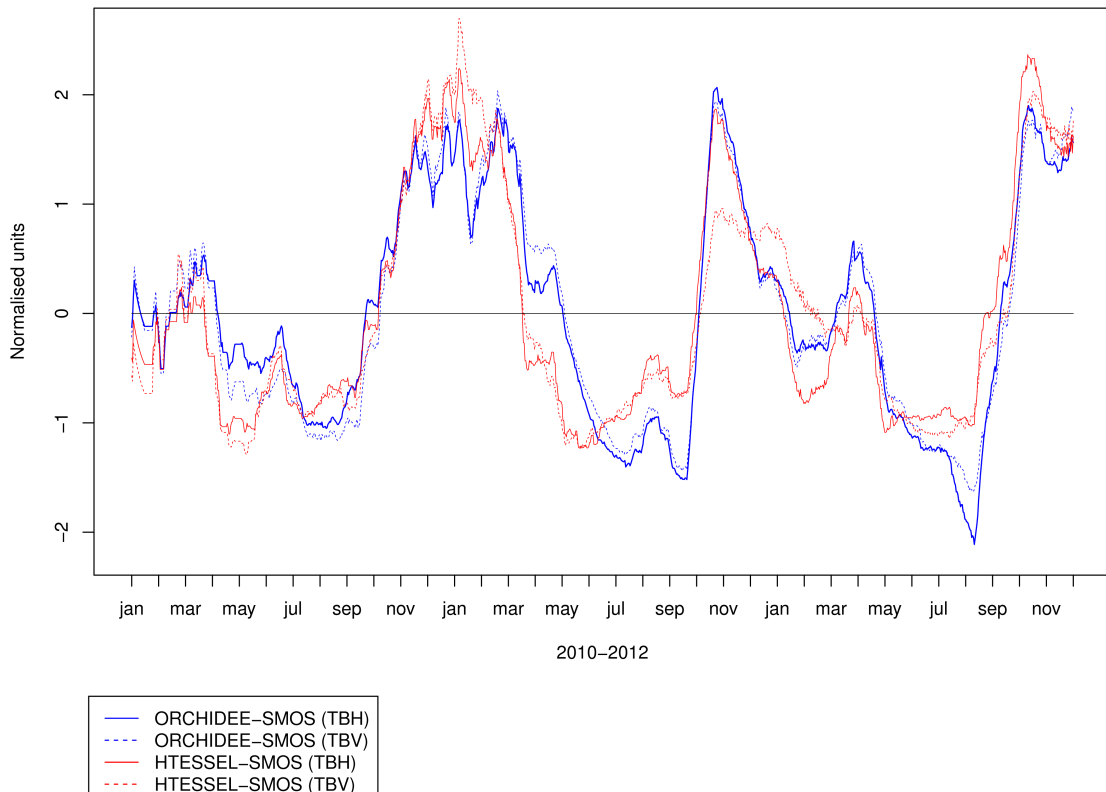
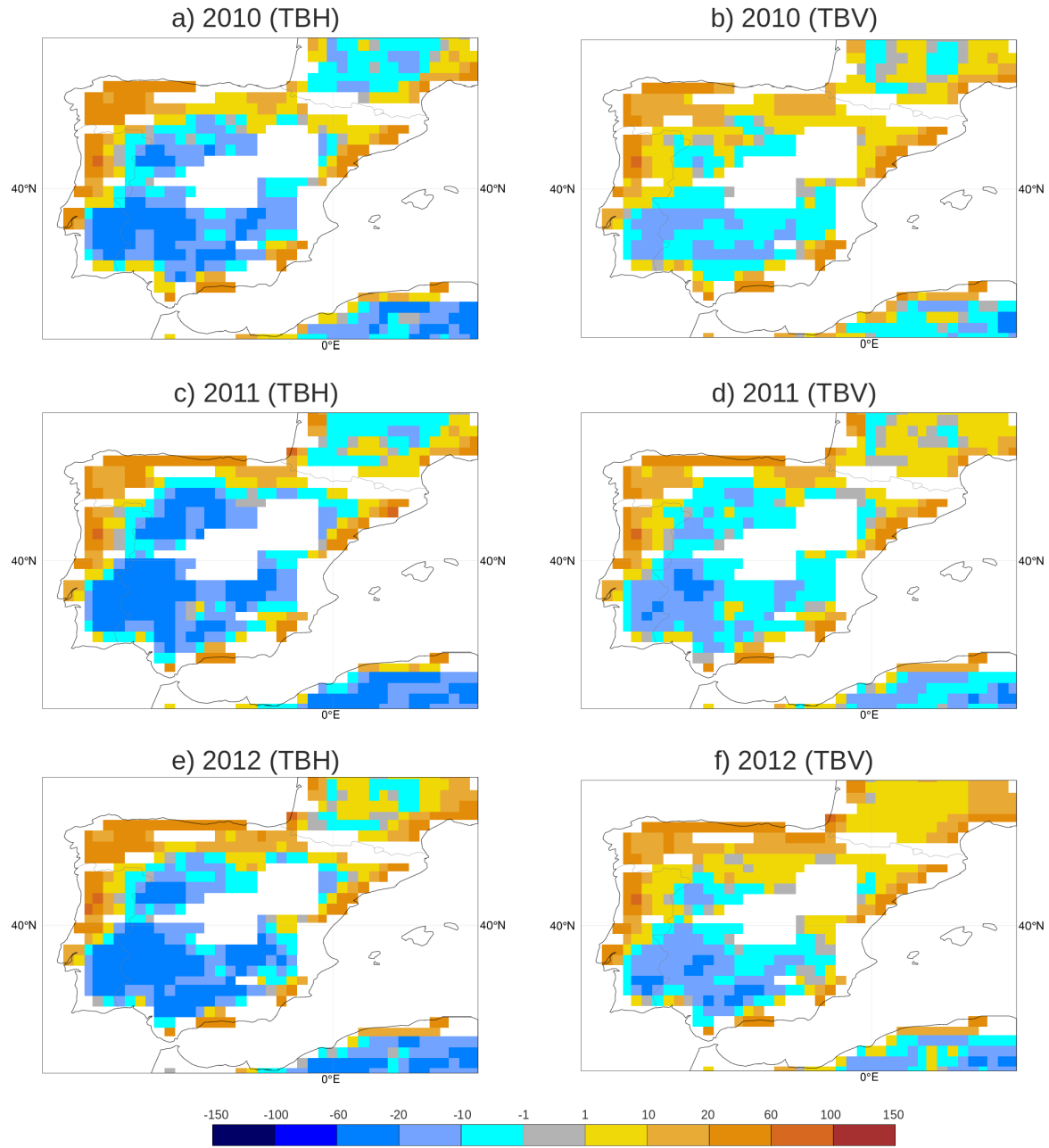


Figure 4: Spatial patterns associated with the first two EOF variation modes (P1 and P2) of the difference between modelled TB (H-TESSEL) and measured TB (SMOS). TBH and TBV correspond to the horizontal and vertical polarizations, respectively. The percentage of variance explained by each mode is included in brackets.



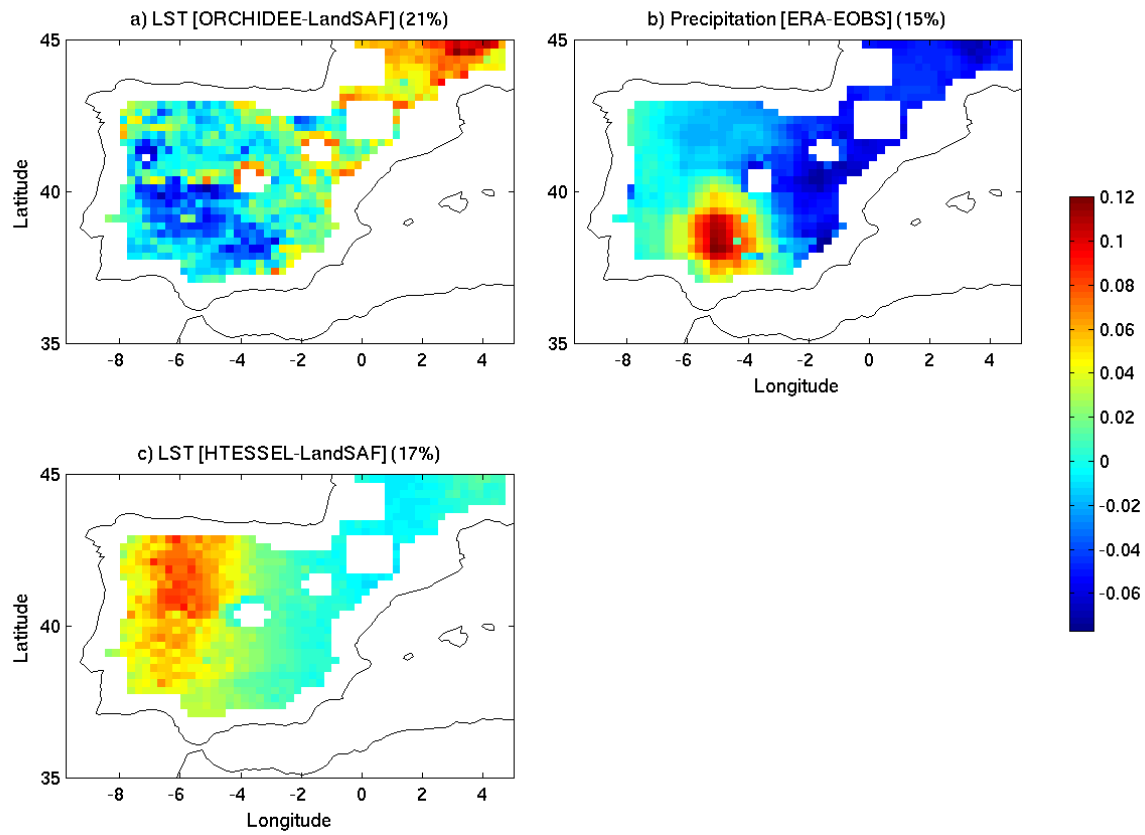
1
2



3
4
5
6
7
8

Figure 6: ECMWF's mean first guess departure (observation-model [K]) from the months of November 2010 to 2012. TBH and TBV correspond to the horizontal and vertical polarizations, respectively.

1
2

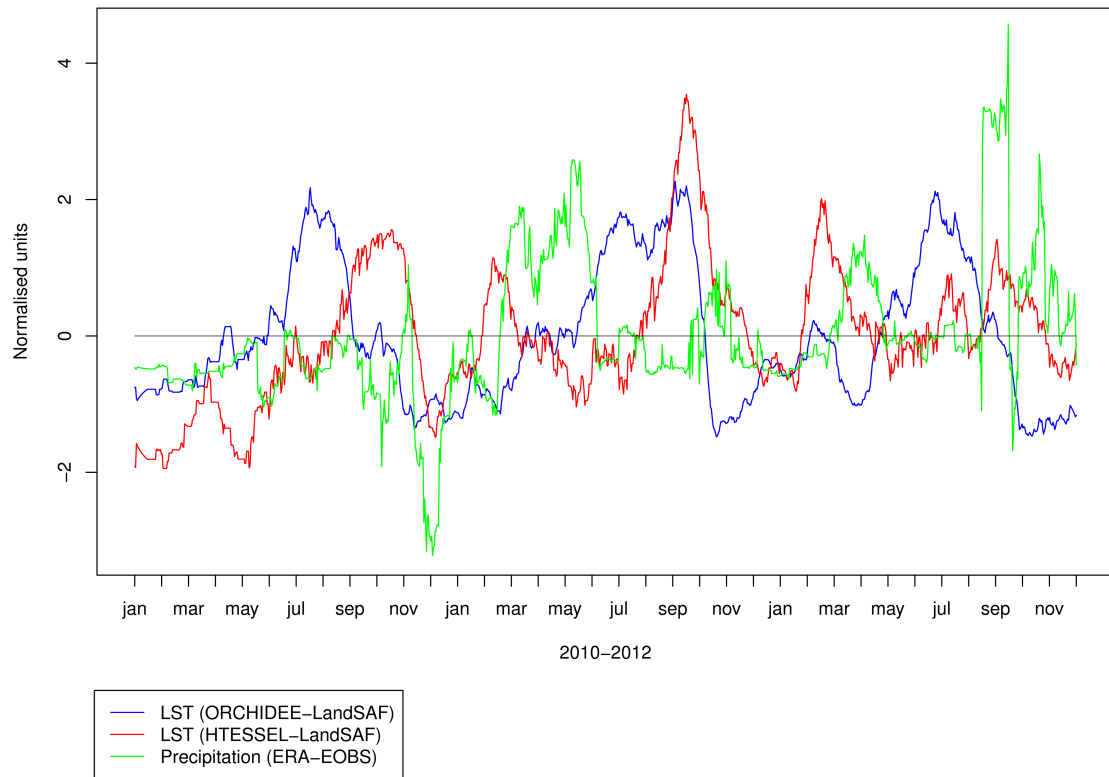


3

4 Figure 7: Spatial patterns from the first EOF variation mode of the LST and the precipitation
5 errors. The percentage of variance explained by each mode is included in brackets.

6
7
8
9
10
11
12
13
14

1
2



3

Figure 8: Temporal evolution of the expansion coefficients correspondent to the first EOF variation mode of the LST and the precipitation errors. As in Fig. 5, values have been normalised using the standardization method.

7

8

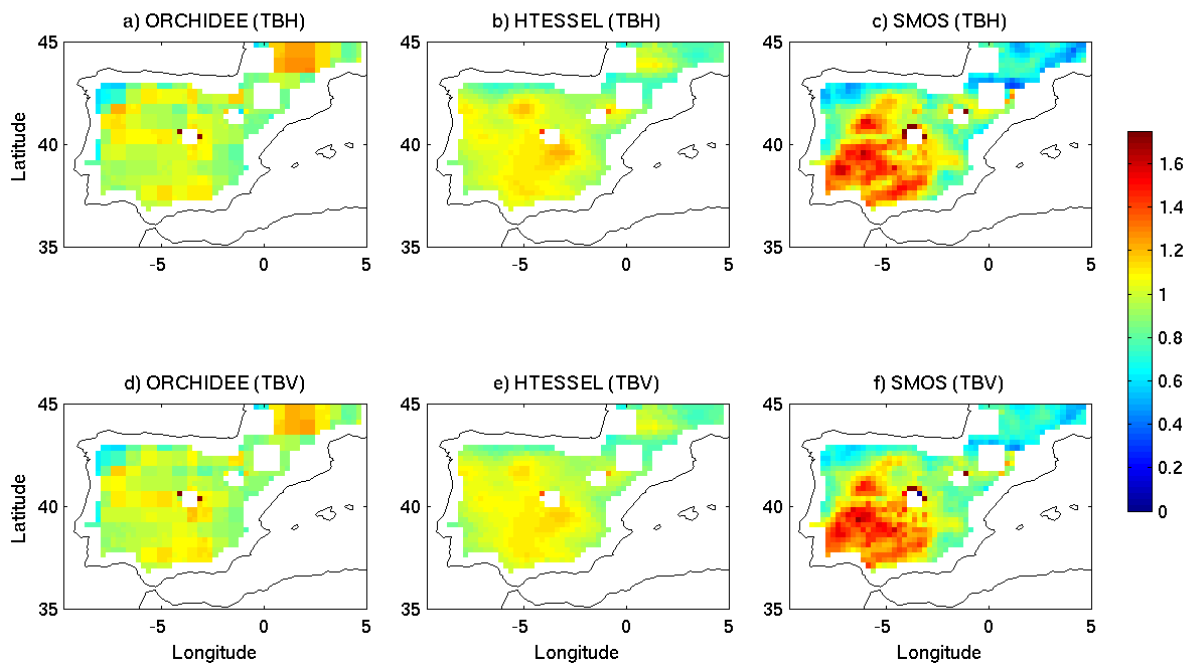
9

10

11

12

13



3
4 Figure 9: Normalised amplitude of the smoothed annual cycle of modelled and measured
5 TBS: $\frac{\text{amplitude (TB)}}{\text{TB}}$. TBH and TBV correspond to the horizontal and vertical polarizations,
6 respectively.

1
2

